Yunhuan Sui
Haiqing Lu
Xingzhong Zhang ✉
Mengqin Shen

https://doi.org/10.21278/TOF.494074424
ISSN 1333-1124
eISSN 1849-1391

STUDY ON BULGING DEFORMATION OF 0Cr18Ni9 STAINLESS STEEL CONTINUOUSLY CAST SLAB BASED ON HIGH-TEMPERATURE CREEP PROPERTY

Summary

In this paper, high-temperature tensile creep tests were conducted at 1,050 °C, 1,100 °C and 1,150 °C under different stresses. The high-temperature mechanical properties and creep behaviour of continuously cast slab made of 0Cr18Ni9 stainless steel were obtained, and the creep constitutive equation was fitted. Based on this, bulging deformation of a three-dimensional slab model was simulated. The results showed that the maximum bulging deformation of the wide side and the narrow side along the casting direction were approximately 1.7 times and 1.3 times larger than the deformation when creep was not considered, respectively. By changing the roller pitch, it was found that the larger the roller pitch was, the larger the bulging deformation of the wide side and the larger the creep deformation proportion was. Similarly, the bulging deformation and the creep deformation proportion in the narrow side also increased with the increasing of the roller pitches, but the increments were not significant.

Key words: *mechanical property of steel; high-temperature tensile creep test; creep constitutive equation; bulging deformation; continuous casting*

1. Introduction

When a metal is at a temperature of 0.3-0.4 times of its own melting point, the creep phenomenon is very obvious, and the creep rate is also significantly accelerated [1-2]. During the process of continuous casting, steel undergoes the process of solidification from liquid to solid state, accompanied by bending and straightening deformation. The minimum slab surface temperature is far greater than 900 °C (much more than 0.4 times the melting point of most low alloy steels), therefore, creep deformation of a continuously cast slab should not be neglected [3]. In addition, because the shell of a slab is in the nonuniform temperature field and is affected by the static pressure of molten steel, bulging deformation occurs between the adjacent rollers, which is the main reason for the defects such as internal cracks and intermediate segregation. Due to various factors affecting the bulging deformation in continuous casting processes, it is difficult to obtain the bulging deformation data by measurement. Only a few papers provided the measurement data [4-5].

For many years, finite element method simulation is widely used to analyse and calculate bulging deformation of continuously cast slabs. Grill and Schwerdtfeger [6] established a two-dimensional model to calculate the bulging deformation of a slab, but ignored the constraint of the narrow edge on bulging deformation, which could not guarantee the calculation accuracy. Three different creep models were used to calculate the bulging deformation based on the same two-dimensional model, and the results were significantly different [7]. A three-dimensional model was developed by Okamura et al. [8] to investigate bulging deformation and bulging strains near the narrow side. Sheng and Sun et al. [9-10] put forward that bulging deformation and bulging strains were composed of elastic strain and creep strain. The elastic strain was mainly caused by shell stress. Qin et al. [11-12] calculated and compared bulging deformation based on 2D and 3D finite element models, and proposed an improved 3D finite element model to simulate bulging deformation. Ma et al. [13] took a wide-thick slab continuous casting machine in a steel plant as the research object and simulated the bulging deformation of Q345E steel at three typical casting flow positions during the continuous casting process. The effect of creep was taken into account for the calculation and analysis of bulging deformation in the above-mentioned studies. In recent years, oriented silicon steel and Q235B steel were taken as the research object by Liu et al. [14] and Zhao [15], respectively, where the bulging deformations at the solidification end zone of the cast slab under different pulling speeds were calculated using empirical formulae.

Steel has been a focus of research for many years [16-18]. Austenite stainless steel 0Cr18Ni9, as heat-resistant steel, is widely used in food industry and for chemical equipment due to its good chemical stability and high strength. It was also welded with other dissimilar metals to give full play to the complementary advantages of the two materials [19-20]; or used as interlayer to improve the diffusion bonding quality of Ti-6Al-4V alloy (TC4) and oxygen-free copper (OFC) [21]. Free-machining element Te was added to 0Cr18Ni9 steel to improve its machinability and mechanical properties [22]. When it comes to the research into the elevated temperature in the past decade, some relevant papers dealing with steel can be found. Chen et al. [23-24] studied the creep behaviour and fatigue crack growth of steel at 550 °C. High-temperature tensile tests at different strain rates in the temperature range from 500 to 850 °C were carried out to study the hot deformation behaviour of steel [25]. Li et al. [26] conducted tensile tests in the range from 20 to 1,200 °C to investigate the effect of temperature on the tensile properties, and the mechanical property parameters such as elastic modulus, yield stress and tensile strength were obtained.

However, the research on creep behaviour of 0Cr18Ni9 stainless steel continuously cast slabs at high temperature is insufficient. Therefore, a tensile creep test of a 0Cr18Ni9 continuously cast slab at high temperature was performed in this study. According to the test results, the creep constitutive equation was fitted, and a three-dimensional shell model was established to simulate the bulging deformation of the slab. The bulging deformation of the wide side and the narrow side were calculated and compared in two cases, i.e. in one case creep was considered and in another it was not considered. Then, the roller pitch was changed, and the bulging deformation of the wide side and the narrow side between different roller distances were obtained.

2. Materials and methods

In this study, the specimens for the tensile test were machined from a continuously cast slab made of 0Cr18Ni9 stainless steel, which was produced by a steel mill. The chemical composition of the steel is listed in Table 1.

According to the dimensional requirement of a Gleeble-3800 thermal-mechanical physical simulation machine for tensile specimens, a bar 10 mm in diameter and 120 mm in length with screw threads on both ends was used, as shown in Fig. 1.

Table 1 Chemical composition of stainless steel 0Cr18Ni9 (wt. %)

C	Si	Mn	S	P	Cr	Ni	Fe
0.07	1.00	2.00	0.03	0.045	18.00	9.00	Balance

Ni-Cr thermocouples were welded in the middle of the specimens to measure and monitor the actual test temperature. In order to simulate the cooling process of the steel continuously cast slab, these specimens were heated at 10 °C/s, held at 1,300 °C for two minutes, then cooled at 3 °C/s to the tensile test temperatures, and finally held for three minutes before stretching [27]. Because the rate of heating or cooling is rapid, which may cause the effects of local hardening, grain refinement, and residual thermal stress on the material properties, it is necessary to hold the specimen at each test temperature for several minutes to ensure the homogeneity in the gauge length. The thermal plastic tests were performed at a constant strain rate of 0.001 /s from 800 °C to 1,200 °C.

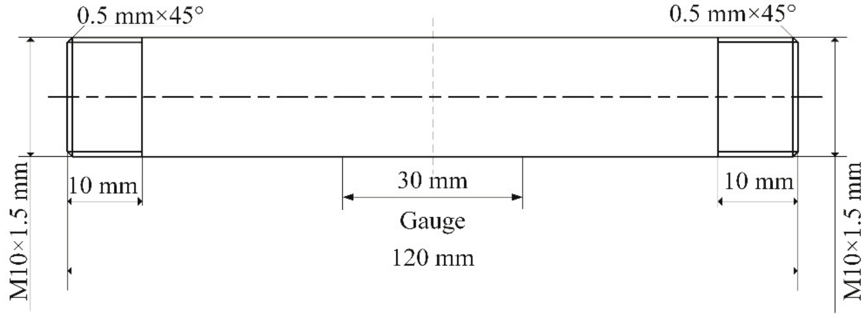

Fig. 1 Tensile test specimen

Based on the test results, the temperature range of the non-plastic zone and the yield strength at each temperature value were obtained. To study the creep property, the tensile stress was set below the yield strength so that merely the creep strain could be collected rather than the plastic strain. The test parameters of the tensile creep test are listed in Table 2. Since the applied stress value is rather small and the temperature outside the gauge of the specimen is lower than that in the middle, the creep strain outside the gauge can be neglected.

Table 2 Parameters of tensile creep test

Temperature /°C	Yield strength /MPa	Applied stress /MPa
1,050	32.62	14.98, 16.23, 16.85, 17.48
1,100	26.37	14.98, 15.61, 16.23, 17.48
1,150	20.87	13.73, 14.98, 16.23, 17.48

3. Results and discussion

3.1 Mechanical properties

Fig. 2 shows a reduction of the area of 0Cr18Ni9 at 800 °C to 1,200 °C, which is an indicator of plasticity. It can be seen that the minimum reduction of the area occurs at 950 °C, and the reduction of the area is higher than 60% from 1,000 °C to 1,150 °C, which indicates good plasticity in this temperature range.

The 0.2 offset yield strength of stainless steel 0Cr18Ni9 in the temperature range from 800 to 1,200 °C is exhibited by the test value curve in Fig. 3 based on the tensile test data.

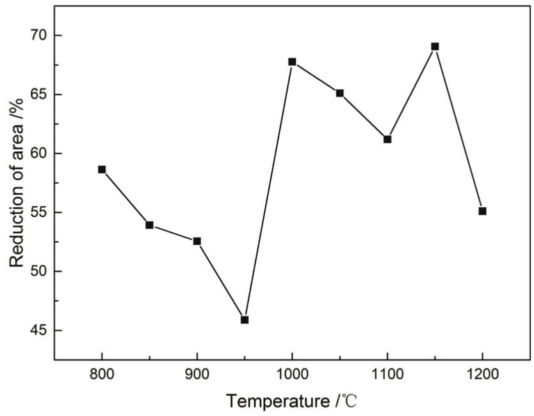

Fig. 2 Reduction of area

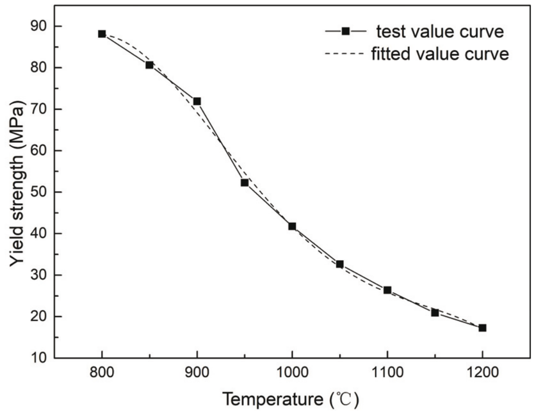

Fig. 3 Yield strength ($R_p0.2$)

It could be observed that the yield strength ($R_p0.2$) decreases rapidly with the increasing temperature. According to the yield strength curve, the relationship between the yield strength and the temperature can be fitted as Equation (1), and the fitted value curve is shown in Fig. 3.

$$y = -1.033\times10^{-8}T^4 + 4.264\times10^{-5}T^3 - 0.065T^2 + 43.655T - 10685.194 \tag{1}$$

Similarly, in terms of the tensile test data, Young's modulus of 0Cr18Ni9 stainless steel at high temperatures can be calculated as shown in Fig. 4.

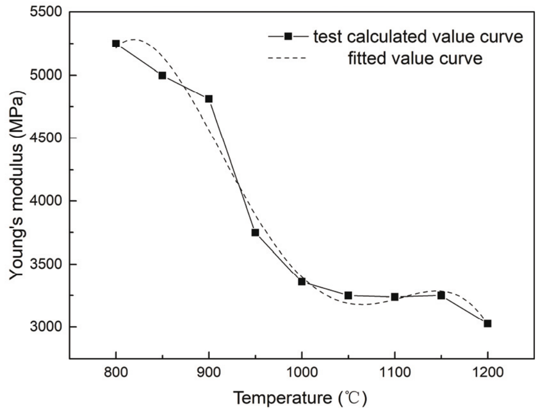

Fig. 4 Young's modulus

The relationship between Young's modulus and temperature can be expressed as Equation (2), and the fitted value curve is also shown in Fig. 4.

$$y = -1.047\times10^{-6}T^4 + 0.004T^3 - 6.346T^2 + 4183.917T - 1.017\times10^{-6} \tag{2}$$

3.2 Creep properties

The creep strain versus time curves at different temperatures and stresses were obtained by fitting the tensile creep test data, as presented in Fig. 5.

It can be seen from Fig. 5 that each curve conforms to the trend of a typical creep curve, and with an increase in temperature and stress, the creep rate increases, the steady-state creep time shortens, and fracture of the specimens appears earlier.

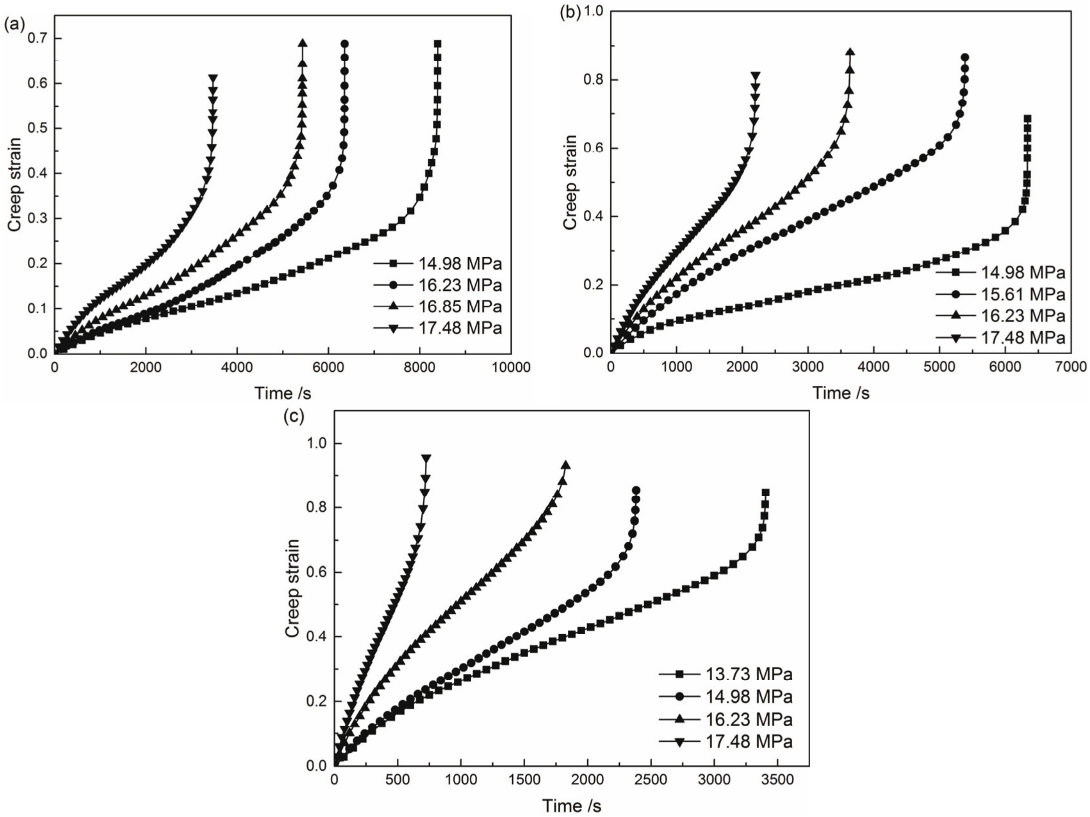

Fig. 5 Tensile creep test curves at (a) 1,050 °C, (b) 1,100 °C, (c) 1,150 °C

Furthermore, the steady-state creep rate and creep breaking time could be obtained under different test conditions as listed in Table 3.

Table 3 Creep parameters under different test conditions

Temperature/°C	Stress σ /MPa	Steady-state creep rate $\dot{\varepsilon}_c$	Creep breaking time t_f/s
1,050	14.98	3.67361E-6	8,395
	16.23	5.84282E-5	6,355
	16.85	6.80723E-5	5,432
	17.48	8.32827E-5	3,469
1,100	13.73	9.94008E-5	6,339
	14.98	1.10918E-4	5,386
	16.23	1.45867E-4	3,638
	17.48	2.22069E-4	2,201
1,150	14.98	1.57496E-4	3,405
	15.61	2.32265E-4	2,383
	16.23	3.72427E-4	1,826
	17.48	5.85092E-4	725

The power-law creep equation [28] expressed as Equation (3) is simplified from the Mukherjee-Bird-Dorn equation [29], which is put forward on the basis of the microscopic mechanism of the material. It is considered that the creep at a high temperature is mainly a diffusion phenomenon and is appropriate for high temperature creep conditions.

$$\dot{\varepsilon}_c = A\sigma^n \exp\left(-\frac{Q_c}{RT_h}\right) \tag{3}$$

where A is the dimensionless constant related to the microstructure of the material; Q_c is the apparent activation energy, J; R is the gas Avogadro constant, 8.314 J/mol; T_h is the thermodynamic temperature, K; and $\dot{\varepsilon}_c$ is the rate of steady-state creep.

Taking the logarithm on both sides of Equation (3), Equation (4) is obtained as follows:

$$\ln\dot{\varepsilon}_c = \ln A + n\ln\sigma - \frac{Q_c}{RT_h} \tag{4}$$

It can be found that Equation (4) is transformed into a general linear equation when $\ln\dot{\varepsilon}_c$ is the dependent variable and $\ln\sigma$ is the independent variable. The relationship between $\ln\dot{\varepsilon}_c$ and $\ln\sigma$ is shown in Fig. 6.

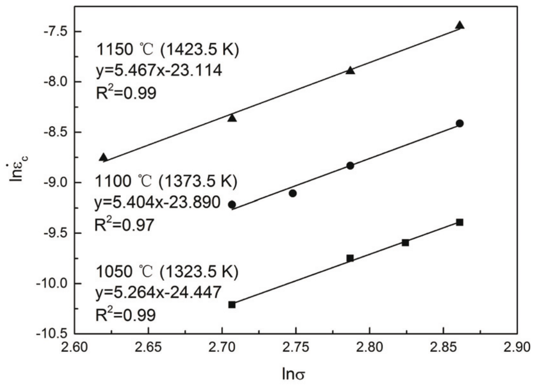

Fig. 6 Relationship between $\ln\dot{\varepsilon}_c$ and $\ln\sigma$

Fig. 6 shows that there is a good linear relationship between the logarithmic stress and the logarithmic steady-state creep rate. The slope of the line given in Fig. 6 is the value of n. The stress index n is averaged and the value of 5.38 is appropriate.

Similarly, in Fig. 7, the reciprocal of the temperature and the logarithmic steady-state creep rate also describes a good linear relationship.

The average calculation of -Qc/R indicates that the apparent activation energy Qc is 289.7 KJ/mol. When the parameters n and Qc are determined, A is calculated in terms of the steady-state creep rate values, and the average value of A is 4.57×10^6.

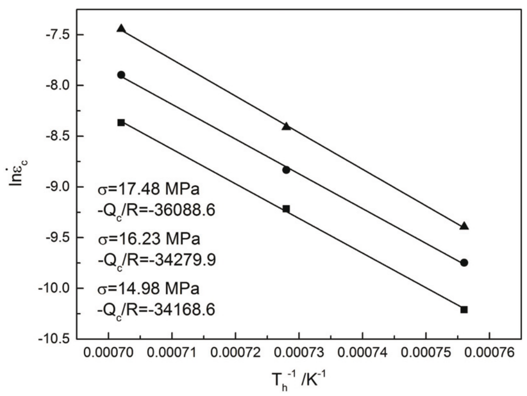

Fig. 7 Relationship between $\ln\dot{\varepsilon}_c$ and $1/T_h$

Therefore, the constitutive equation of the 0Cr18Ni9 stainless steel for the creep rate at a high temperature can be expressed as Equation (5).

$$\dot{\varepsilon}_c = 4.57\times10^6\sigma^{5.38}\exp\left(-\frac{34845.7}{T_h}\right) \tag{5}$$

Furthermore, to obtain the constitutive equation between stress and strain, Equation (6) [30] is taken as reference.

$$\varepsilon_c = \frac{1}{a+bt^{c-1}} \tag{6}$$

where a, b and c are all parameters related to temperature and stress. The tensile creep test data were taken into Equation (6) to calculate the values of the parameters a, b, and c under different test conditions. The relationship between $\ln\left(\frac{\dot{\varepsilon}_c}{A}\right)$ and $1/a$, $1/b$, c is shown in Fig 8.

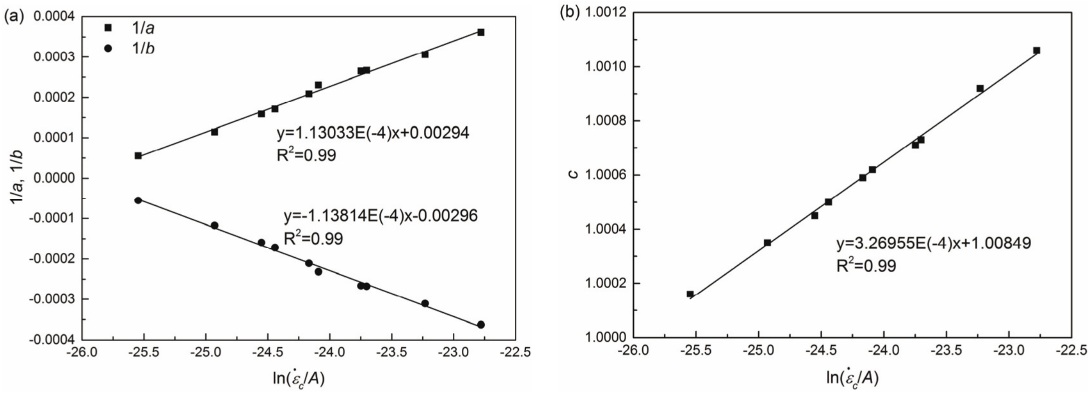

Fig. 8 Relationship between $\ln(\dot{\varepsilon}_c/A)$ and parameters (a) $1/a$, $1/b$, (b) c

Fig. 8 reveals that there is an apparent linear relationship between $\ln(\dot{\varepsilon}_c/A)$ and $1/a$, $1/b$, c. It could be seen from the correlation coefficient that the fitting effect is good. The expressions of $1/a$, $1/b$ and c are shown as Equations (7) to (9).

$$\frac{1}{a} = 0.00294 + 1.13033E(-4)\ln\left(\sigma^{5.38}\exp\left(-\frac{34845.7}{T_h}\right)\right) \tag{7}$$

$$\frac{1}{b} = -0.00296 - 1.13814E(-4)\ln\left(\sigma^{5.38}\exp\left(-\frac{34845.7}{T_h}\right)\right) \tag{8}$$

$$c = 1.00849 + 3.26955E(-4)\ln\left(\sigma^{5.38}\exp\left(-\frac{34845.7}{T_h}\right)\right) \tag{9}$$

The creep constitutive equation of the 0Cr18Ni9 stainless steel was obtained by substituting the expressions of a, b, c into Equation (6). Then, the test data were compared with the calculated values based on Equation (6), as presented in Fig. 9.

In Fig. 9, the dash line represents the calculated value and the solid line represents the test value. It can be observed that in the first stage of creep, the calculated values obtained from the fitted creep constitutive equation are greater than the test values, while in the steady-state creep stage, the calculation values and the test values are close to each other.

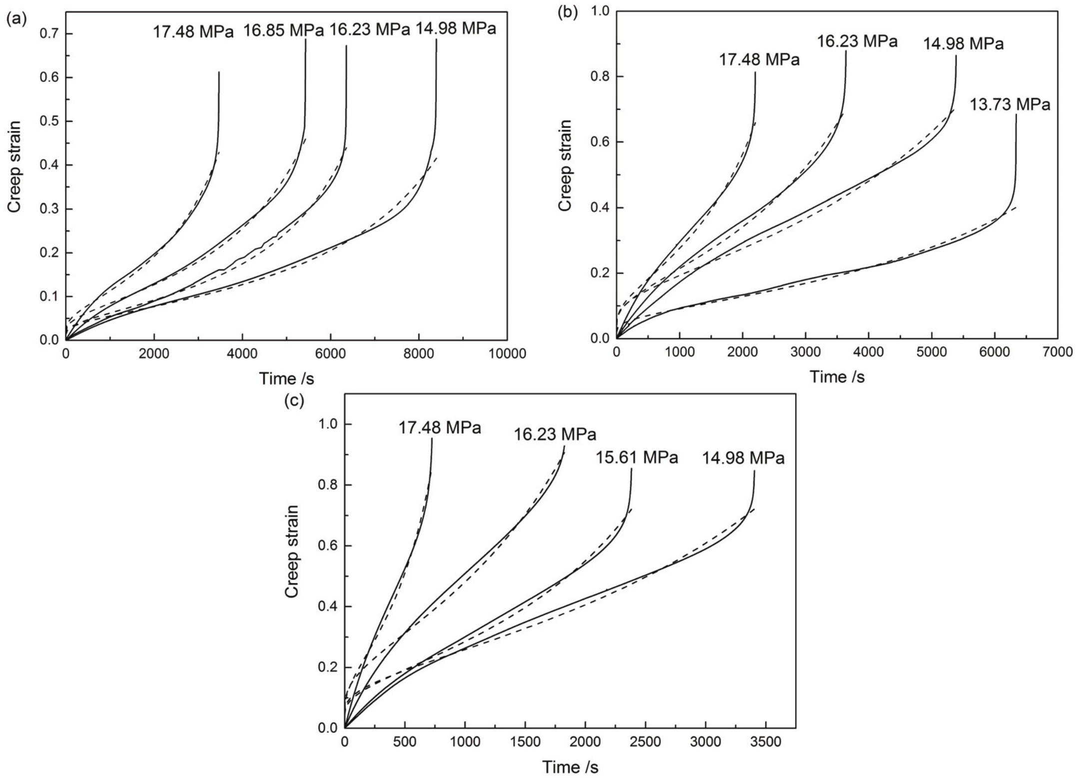

Fig. 9 Comparison between test value and calculated value: (a) 1,050 °C, (b) 1,100 °C, (c) 1,150 °C

Due to the very small proportion of the first creep stage at high temperatures, the creep constitutive equation can be used to describe the creep behaviour of the first two stages, especially of the second creep stage.

3.3 Bulging deformation of continuously cast slab

3.3.1 Model and relevant parameters

To simulate the bulging deformation of the 0Cr18Ni9 continuously cast slab, the roller arrangement and the cooling schedule of a R9300 vertical-arc continuous caster of one steel mill is taken as reference. Fig. 10 illustrates the upper part of this caster.

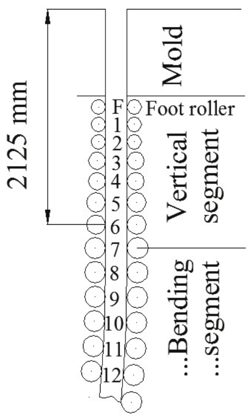

Fig. 10 Calculation location of bulging deformation

In this study, the position between roller 6 and roller 7 was studied. Roller 6 is at the end of the vertical segment, which is 2,125 mm from the top of the mould, and the continuously cast slab begins to be bent from here. The diameters of rollers 6 and 7 are 200 mm, and the pitch is 240 mm.

For the convenience of the simulation, a reasonable simplification and assumptions are made for a three-dimensional continuously cast slab model as follows:

(1) The liquid core of the continuously cast slab is omitted, then it simplifies into a cavity shape. The static pressure of the molten steel is loaded onto the inner wall.

(2) The rollers are considered as rigid bodies.

(3) As the symmetry in shape and size of the continuously cast slab, the three-dimensional finite element model is 1/4 of the slab between two rollers. The shell thickness is 22 mm, and the slab length is 240 mm, as shown in Fig. 11. The element size is 5 mm × 5 mm × 4.4 mm.

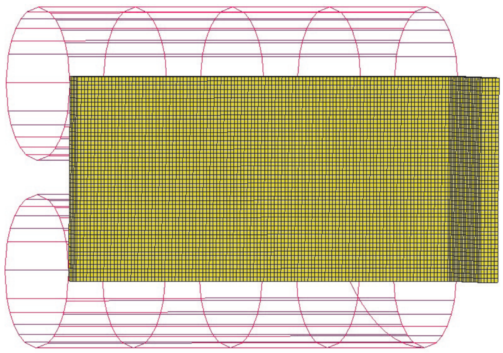

Fig. 11 Three-dimensional finite element model of slab

(4) The temperature of the cast slab does not change much along the direction of the casting flow within one roller pitch, so the heat transfer along the direction of the slab moving is neglected, and only the temperature change along the thickness direction of the cast slab is considered.

(5) The coefficient of heat transfer is used to calculate the heat transfer in the secondary cooling zone.

(6) The deformation of the cast slab satisfies the small deformation theory.

The geometry and casting condition parameters are listed in Table 4. The cooling schedule is shown in Table 5.

Table 4 Relevant simulation parameters

Parameter	Value
Slab size /mm	1,000×230
Metallurgical length /mm	35,862
Steel casting speed /(m min^{-1})	1.5
Working mould length /mm	800
Initial temperature /°C	1,480
Liquidus temperature /°C	1,451
Solidus temperature /°C	1,414.6
Density /(kg m^{-3})	7,930
Thermal expansion coefficient /(°C^{-1})	1.5×10^{-5}

Table 5 Cooling schedule

Roller number (Length/mm)	Loop No.	Location	Water flow rate/ (m^3 h^{-1})	Air flow rate/ (m^3 h^{-1})
Foot roller (110)	1	Wide surface in and out	9.45	9,000
	2	Narrow surface left and right	1.05	
No. 1-6 (1,215)	3	Wide surface in and out	41.58	
	4	Narrow surface left and right	6.51	

The coefficient of heat transfer between the cooling water and the surface of the slab can be calculated by the empirical Equation (10) based on Table 5.

$$H = 0.58W^{0.451}\left(1 - 0.0075T_w\right) \tag{10}$$

where H is the coefficient of the heat transfer, W/ (m^2 °C); T_w is the temperature of the cooling water, °C; and W is the density of the cooling water, L/ (m^2 s).

The yield strength, Young's modulus, and the creep properties of the material were obtained from the high-temperature tensile test data described above. In addition, Poisson's ratio varying with temperature is illustrated in Fig. 12.

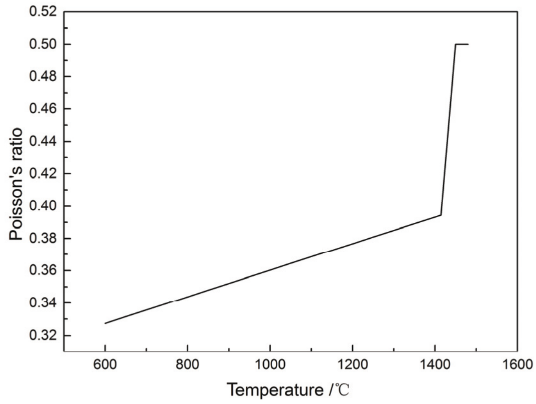

Fig. 12 Poisson's ratio

And the boundary conditions are listed as follows:

(1) The symmetrical displacement constraint was applied on the symmetrical surface of the slab, where both ends were controlled by translate and rotate constraint.

(2) The static pressure of the molten steel was applied to the inner surface of the slab and its value varied with the distance from the meniscus along the direction of casting flow.

(3) The displacement of each element on the front and rear faces of the continuously cast slab is bound to maintain a flat surface.

3.3.2 Creep effect on bulging deformation

The bulging deformation of the continuously cast slab was simulated based on an elastic-plastic model and an elastic-plastic and creep model. Fig. 13 describes the bulging deformation of the wide side centre and the narrow side centre along the casting direction.

It can be seen from Fig. 13 that the trend of the bulging deformation on the wide side centre and the narrow side centre is similar along the casting direction. The curves are of convex distribution. On the wide side, the bulging deformation at the centre of the two rollers is the largest. The maximum bulging deformation based on the elastic-plastic model is 1.155 mm, while the maximum bulging deformation based on the elastic-plastic and creep model is 1.981 mm, which is about 1.7 times the size of the former model. Because the stress did not reach the yield point there is no plastic deformation. The maximum creep deformation is considered as the difference of 0.826 mm. Fig. 13(b) shows that the maximum bulging deformation based on the elastic-plastic and creep model is 0.47 mm, which is about 1.3 times the size of the former model. And the difference between them is kept at 0.12 mm, which indicates that the creep deformation is about 0.12 mm.

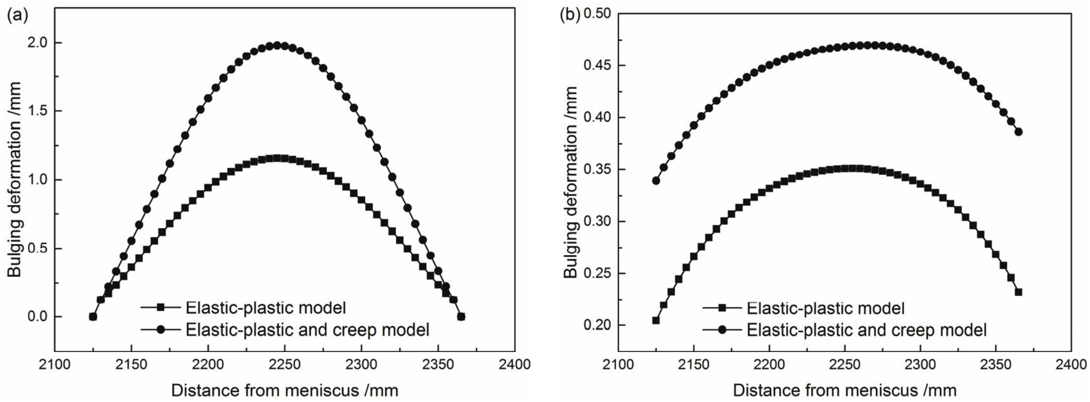

Fig. 13 Bulging deformation along casting direction: (a) wide side centre, (b) narrow side centre

The bulging deformation along the width and the thickness of the slab is illustrated in Fig. 14.

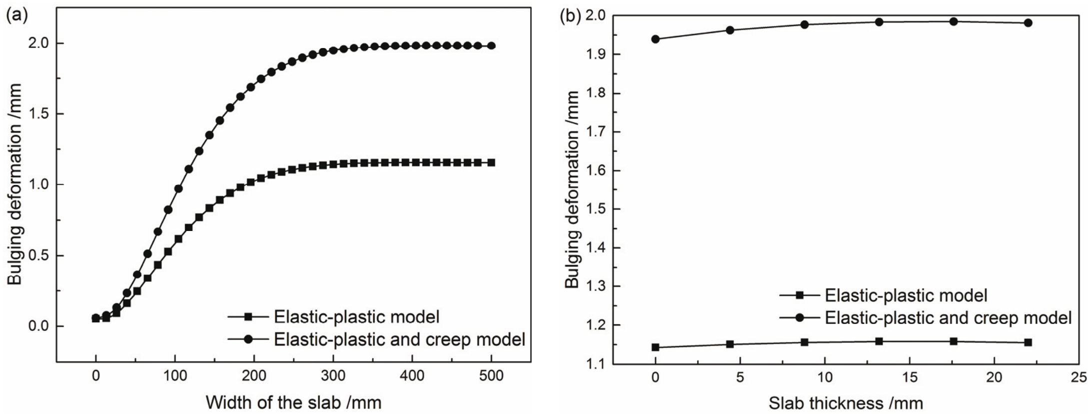

Fig. 14 The bulging deformation of wide side centre along (a) width of the slab, (b) thickness of the slab

Fig. 14(a) reveals that the bulging deformation increases with the increasing distance from the corner of the cast slab, and then it tends to be flat. The corner bulging deformation caused by creep is very small, and the closer to the centre of the wide side, the greater the deformation caused by creep. On the other hand, Fig. 14(b) indicates that the bulging deformation along the thickness of the slab changes very little in both calculation models.

3.3.3 Effect of roller pitch on bulging deformation

Taking the bulging deformation of the wide side centre along the casting direction as an example, the effect of the roller pitch on the bulging deformation was calculated and compared by changing the roller spacing. The bulging deformations of the wide side centre along the casting flow direction, when different roller pitches are used, are shown in Fig. 15.

Fig. 15 illustrates the bulging deformation of the wide side centre along the casting direction with the roller pitches of 180 mm, 200 mm, 220 mm, and 240 mm. Fig. 15(a) shows the case without creep deformation, and the elastic deformation is the bulging deformation. When creep is taken into account in Fig. 15(b), the value of the bulging deformation is the sum of the elastic deformation and the creep deformation. It can be observed from the figure that the minimum bulging deformation occurs at the position where the slab and roller are in contact with each other. The maximum bulging deformation increases when the roller pitch is increased. At the same time, the elastic deformation and the creep deformation also increase. Similarly, the bulging deformation of the narrow side centre with different roller pitches used can also be obtained.

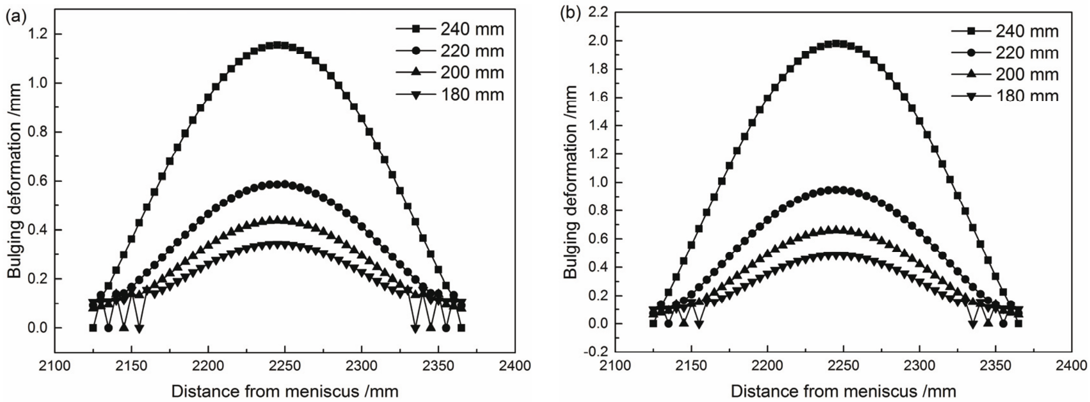

Fig. 15 Bulging deformation with different roller pitches based on (a) elastic-plastic model, (b) elastic-plastic and creep model

To sum up, the elastic deformation, creep deformation and bulging deformation of the wide side centre and the narrow side centre with different roller pitches are listed in Table 6.

Table 6 Deformation with different roller pitches

Roller pitch /mm	Elastic deformation /mm Wide, Narrow side	Creep deformation /mm Wide, Narrow side	Bulging deformation /mm Wide, Narrow side	Proportion of creep deformation/% Wide, Narrow side
180	0.343, 0.316	0.145, 0.085	0.488, 0.401	29.7, 21.2
200	0.437, 0.325	0.222, 0.101	0.659, 0.426	33.7, 23.7
220	0.586, 0.347	0.362, 0.116	0.948, 0.463	38.2, 25.1
240	1.155, 0.351	0.826, 0.119	1.981, 0.47	41.7, 25.3

The bulging deformation of the wide side centre and the narrow side centre along the casting direction increases with the roller pitch increasing, and the proportion of the creep deformation also increases at the same time. But the increment of the creep proportion on the wide side centre is more obvious, and the change on the narrow side centre is relatively small.

4. Conclusions

According to the tensile test at high temperatures, stainless steel 0Cr18Ni9 has the lowest plasticity at 950 °C, and higher plasticity in the temperature range from 1,000 °C to 1,150 °C. The creep test results show that with an increase in temperature and stress, the creep rate increases, the steady-state creep time shortens, and fracture of the specimens appears earlier.

The bulging deformation of the wide side is more obvious than that of the narrow side. The maximum bulging deformation of the wide side centre along the casting direction is about 1.7 times the size of that when creep is not considered. When it comes to the narrow side centre, the bulging deformation is about 1.3 times the size of that when creep is not considered.

With the roller pitch increasing, the bulging deformation of the wide side centre increases, and so does the bulging deformation of the narrow side centre. At the same time, the proportion of the creep deformation on the wide side increases obviously. This indicates that the calculation results can be more accurate when the creep deformation is taken into account.

Acknowledgments

This study was supported by the Weifang University PhD Research Start-up Foundation (grant No. 2023BS34) and the Talent project (Development of internal combustion generator set based on low carbon fuel (ammonia+hydrogen)).

REFERENCES

[1] Ottosen, N.S.; Ristinmaa M. The mechanics of constitutive modelling, *Elsevier: Amsterdam*, *Holland*, **2005**; 387-388. https://doi.org/10.1016/B978-008044606-6/50026-6

[2] Ashby, M.F.; Jones, D.R.H. Engineering materials 1: an introduction to properties, applications and design, *Elsevier: New York, USA*, **2012**; 312-313. https://doi.org/10.1016/B978-0-08-096665-6.00001-5

[3] Brimacombe, J.K.; Sorimachi, K. Crack formation in the continuous casting of steel, *Metallurgical Transactions B* **1997** *8B*, 489-505. https://doi.org/10.1007/BF02696937

[4] Yoon, U.-S.; Bang, I.-W.; Rhee, J.-H.; Kim, S.-Y.; Lee, J.-D.; Oh, K.-H. Analysis of mold level hunching by unsteady bulging during thin slab casting, *ISIJ International* **2002** *42*, 1103-1111. https://doi.org/10.2355/isijinternational.42.1103

[5] Miranda, R.; Barron, M.A.; Barreto, J.; Hoyos, L.; Gonzalez, J. Experimental and numerical analysis of the free surface in a water model of a slab continuous casting mold, *ISIJ International* **2005** *45*, 1626-1635. https://doi.org/10.2355/isijinternational.45.1626

[6] Grill, A.; Schwerdtfeger, K. Finite-element analysis of bulging produced by creep in continuously cast steel slabs, *Ironmaking and Steelmaking* **1979** *6*,131-135.

[7] Ha, J.-S.; Cho, J.-R.; Lee, B.-Y.; Ha, M.-Y. Numerical analysis of secondary cooling and bulging in the continuous casting of slabs, *Journal of Materials Processing Technology* **2001** *113*, 257-261. https://doi.org/10.1016/S0924-0136(01)00654-9

[8] Okamura, K.; Kawashima, H. Three-dimensional elasto-plastic and creep analysis of bulging in continuously cast slabs, *ISIJ International* **1989** *29*, 666-672. https://doi.org/10.2355/isijinternational.29.666

[9] Sheng, Y.-P.; Sun, J.-Q.; Zhang, M. Calculation for bulging deformation of continuously casted slab, *Iron and Steel* **1993** *28*, 20-25. http://dx.doi.org/10.13228/j.boyuan.issn0449-749x.1993.03.006

[10] Sun, J.-Q.; Sheng, Y.-P.; Zhang, X.-Z. Analysis of bulging deformation and stress in continuous cast slabs, *Journal of Iron and Steel Research* **1996** *1*, 11-15.

[11] Qin, Q.; Shang, S.; Wu, D.-P.; Zang, Y. Comparative analysis of bulge deformation between 2D and 3D finite element models, *Advances in Mechanical Engineering* **2014** *6*, 1-10. http://dx.doi.org/10.1155/2014/942719

[12] Qin, Q.; Huang, J.-L.; Zang, Y. Improvement of three-dimensional bulge deformation model for continuous casting slab, *Journal of Manufacturing Processes* **2020** *55*, 57-65. https://doi.org/10.1016/j.jmapro.2020.03.038

[13] Ma, X.-T.; Wu, C.-H.; Xie. X.; Wu, G.-R.; Zhang, M.; Zeng, J.-H.; Ji, C. Investigation on the bulging deformation of continuously cast wide-thick slab with numerical calculation method, *Iron Steel Vanadium Titanium* **2021** *42*, 106-112.

[14] Liu, H.-J.; Shi, P.-Z.; Xie, J.-F.; Xu, G.-J.; Zhou, J.-J.; Qiu, S.-T. Research on technology of raising casting speed of conventional slab of oriented silicon steel, *Continuous Casting* **2024** *05*, 73-81. http://dx.doi.org/10.13228/j.boyuan.issn1005-4006.20230136

[15] Zhao, J. Research on the deformation of slab in solidification end zone and the setting of roll gap, *Heavy machinery* **2023** *5*, 60-64. http://dx.doi.org/10.13551/j.cnki.zxjxqk.2023.05.018

[16] Sui, Y.-H; Zhang, X.-Z.; Guo, L.; Xu, D.-F. Microstructural study of high temperature creep in Q460E steel based on the solidification method, *Transactions of FAMENA* **2019** *43*(4), 81-90. https://doi.org/10.21278/TOF.43407

[17] Fan, Q.-H.; Gao, H.-W.; Chu, Z.-B.; Zhang, Y.-X.; Cui, Y.-N.; Wang, W.-Z. Hot compression test and microstructure evolution in LZ50 AXLE Steel, *Transactions of FAMENA* **2022** *46*(2), 37-53. https://doi.org/10.21278/TOF.462036921

[18] Topilla, L.; Toros, S. Analysis of the fracture behaviour of dual-phase steels using the Gissmo and Johnson-cook models, *Transactions of FAMENA* **2023** *47*(3), 79-95. https://doi.org/10.21278/TOF.473040522

[19] Wang, J; Feng, Y.; Li, H.; Yang, J.; Yang, H.-T.; Zhang, F.-Q. Microstructure and mechanical properties of TC4/0Cr18Ni9 joint prepared by transient liquid phase diffusion bonding, *Materials Research Express* **2019** *6*, 1065d6. https://doi.org/10.1088/2053-1591/ab3fde

[20] Huang, B.-S.; Liu, J.-Q.; Zhang, S.-S.; Chen, Q.; Chen, L.-Z. Effect of post-weld heat treatment on the residual stress and deformation of 20/0Cr18Ni9 dissimilar metal welded joint by experiments and simulations, *J. Mater. Res. Technol.* **2020**, *9*(3), 6186-6200. https://doi.org/10.1016/j.jmrt.2020.04.022

[21] Shen, Q.; Xiang, H.-Y.; Luo, Q.-Q.; Su, X.-P.; Zhang, L.-M. Interfacial microstructure and mechanical properties of diffusion bonded TC4/0Cr18Ni9/Oxygen Free Copper joints, *Materials and Design* **2013** *50*, 230-234. http://dx.doi.org/10.1016/j.matdes.2013.01.042

[22] Xie, J.-B.; Fan, T.; Sun, H.; Zeng, Z.-Q.; Fu, J.-X. Enhancement of Impurity, Machinability and Mechanical Properties in Te-Treated 0Cr18Ni9 Steel, *Metals and Materials International* **2021** *27*, 1416-1427. https://doi.org/10.1007/s12540-019-00545-3

[23] Chen, L.-J.; Chen, B.; Liu, J.-Z.; Hu, B.-R. Tensile creep behaviour and creep crack propagation of 0Cr18Ni9 at 550 °C, *Proceedings of the 7th National Conference on pressure vessels*, Wuxi, China, **2009** pp. 294-298

[24] Chen, L.J.; Chen, B.; Liu, J.Z.; Hu, B.R. Fatigue crack growth behaviour of 0Cr18Ni9 stainless steel at high temperatures, *Journal of Mechanical Strength* **2012** *34*, 298-302. https://doi.org/10.16579/j.issn.1001.9669.2012.02.013

[25] Wang, X.-T.; Wu, H.-B.; Liu, H.; Niu, G.; Gu, Y.; Wang, C. Study on hot deformation behaviour of austenite stainless steel, *Hot Working Technology* **2019** *48*, 31-34. https://doi.org/10.14158/j.cnki.1001-3814.2019.22.008

[26] Li, W.-F.; Niu, W.; Hao, Z.-M.; Li, M.-H. The effect of temperature on the tensile properties of steel 0Cr18Ni9, *Materials Science Forum* **2010** *654-656*, 194-197. https://doi.org/10.4028/www.scientific.net/MSF.654-656.194

[27] Di, H.-S.; Kang, X.-D.; Wang, G.-D.; Liu, X.-H. High temperature mechanical properties of low carbon steel, *Journal of Northeast University* (*Nature Science*) **2004** *25*, 40-43. https://doi.org/10.3321/j.issn:1005-3026.2004.01.011

[28] Reis, A.G.d.; Reis, D.A.P.; Abdalla, A.J.; Otubo, J. High-temperature creep resistance and effects on the austenite reversion and precipitation of 18Ni(300) maraging steel, *Materials Characterization* **2015** *107*, 350-357. http://dx.doi.org/10.1016/j.matchar.2015.08.002

[29] Mukherjee, A.K. An examination of the constitutive equation for elevated temperature plasticity, *Materials Science and Engineering A* **2002** *322*, 1-22. https://doi.org/10.1016/S0921-5093(01)01115-7

[30] Yang, C.-J.; Chen, J.-B. The constitutive relationship of elevated temperature creep of 40Cr steel, *Journal of Shanghai Jiaotong University* **2012** *46*, 301-305. https://doi.org/10.16183/j.cnki.jsjtu.2012.02.025

Submitted: 20.12.2024
Accepted: 26.4.2025

Yunhuan Sui
suiyunhuan123@163.com
School of Machinery and Automation, Weifang University, Weifang 261061, Shandong, P. R. China
Haiqing Lu
School of Machinery and Automation, Weifang University, Weifang 261061, Shandong, P. R. China
Xingzhong Zhang*
National Engineering Research Centre for Equipment and Technology of Cold Strip Rolling, Yanshan University, Qinhuangdao 066004, Hebei, P. R. China
Mengqin Shen
Shandong Suly Power Technology Co.,Ltd., Weifang 261061, Shandong, P. R. China
*Corresponding author:
zhangxzh@ysu.edu.cn